# Nanoelectronics and Its New Materials – A NEW ERA OF NANOSCIENCE

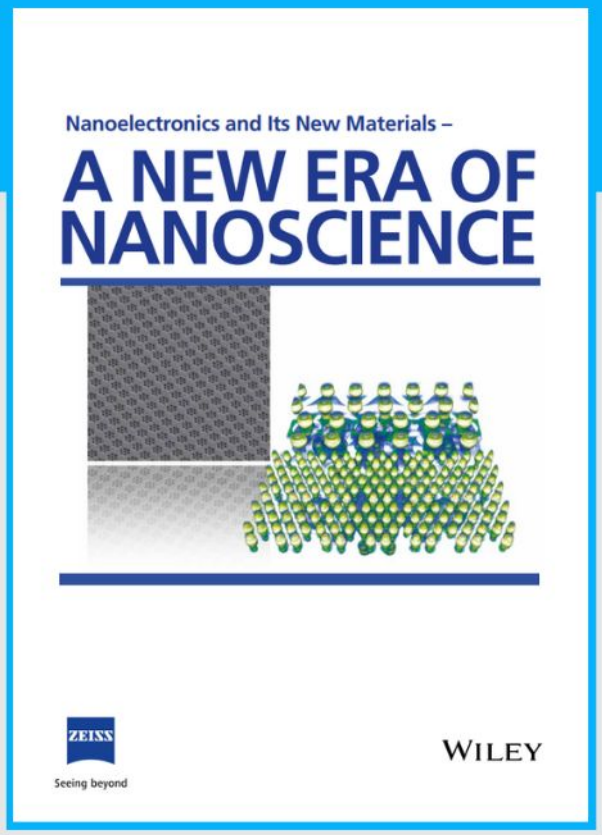


**Discover the recent advances in electronics research and fundamental nanoscience.**

Nanotechnology has become the driving force behind breakthroughs in engineering, materials science, physics, chemistry, and biological sciences. In this compendium, we delve into a wide range of novel applications that highlight recent advances in electronics research and fundamental nanoscience. From surface analysis and defect detection to tailored optical functionality and transparent nanowire electrodes, this eBook covers key topics that will revolutionize the future of electronics.

To get your hands on this valuable resource and unleash the power of nanotechnology, simply download the eBook now. Stay ahead of the curve and embrace the future of electronics with nanoscience as your guide.

ZEISS

Seeing beyond

WILEY

NANO · MICRO small
www.small-journal.com

# Butyrate Modification Promotes Intestinal Absorption and Hepatic Cancer Cells Targeting of Ferroptosis Inducer Loaded Nanoparticle for Enhanced Hepatocellular Carcinoma Therapy

*Yinglan Yu, Xinran Shen, Xin Xiao, Lian Li, and Yuan Huang**

**Sorafenib is an oral-administered first-line drug for hepatocellular carcinoma (HCC) treatment. However, the therapeutic efficacy of sorafenib is relatively low. Here, an oral delivery platform that increases sorafenib uptake by HCC and induces potent ferroptosis is designed. This platform is butyrate-modified nanoparticles separately encapsulated with sorafenib and salinomycin. The multifunctional ligand butyrate interacts with monocarboxylate transporter 1 (MCT-1) to facilitate transcytosis. Specifically, MCT-1 is differentially expressed on the apical and basolateral sides of the intestine, highly expressed on the surface of HCC cells but lowly expressed on normal hepatocytes. After oral administration, this platform is revealed to boost transepithelial transport effectively and continuously in the intestine, drug accumulation in the liver, and HCC cell uptake. Following drug release in cancer cells, sorafenib depletes glutathione peroxidase 4 and glutathione, consequently initiating ferroptosis. Meanwhile, salinomycin enhances intracellular iron and lipid peroxidation, thereby accelerating ferroptosis. In vivo experiments performed on the orthotopic HCC model demonstrate that this combination strategy induces pronounced ferroptosis damage and ignites a robust systemic immune response, leading to the effective elimination of tumors and establishment of systemic immune memory. This work provides a proof-of-concept demonstration that an oral delivery strategy for ferroptosis inducers may be beneficial for HCC treatment.**

## 1. Introduction

Hepatocellular carcinoma (HCC) is one of the most prevalent and lethal cancers worldwide.[1] Surgery is the preferred treatment at the early stage, while HCC is generally diagnosed at an advanced stage.[2] Systemic chemotherapy is necessary for advanced-stage HCC because the poor liver functions of patients limit the possibility of surgical necessity.[3,4] Ferroptosis is a unique iron-dependent method of programmed cell death defined by the aberrant accumulation of lipid peroxides that arrests cancer growth and prompts immunogenic cell death.[5,6] Particularly, ferroptosis is also associated with HCC therapies.[7] Sorafenib (Sor) is the oral-administered first-line chemotherapeutic therapy against advanced-stage HCC, which is also a representative ferroptosis inducer, with the capacity of inducing ferroptosis by indirectly down-regulating glutathione peroxidase (GPX4).[8,9] Although Sor is commonly utilized to treat HCC, the ensuing ferroptosis is still mild because of its poor solubility, low oral bioavailability, nonspecific biodistribution, uncontrollable behavior, low tumor-targeted accumulation, and low therapeutic efficacy.[10–12] Therefore, it is essential to explore alternate strategies capable of enhancing the oral absorption and HCC ferroptosis of Sor.

Oral anticancer nanomedicine is appealing because nanoparticle encapsulation can overcome low medication solubility and shield pharmaceuticals against pH/enzyme destruction in the tough digestive system.[13] But mucus and epithelial cell barriers continue to hinder the oral absorption of the nano-encapsulated medication.[14,15] Our previous studies revealed that microbiota metabolite butyrate anchored polyethylene glycol (PEG) nanoparticles could not impair the mucus-permeability of "mucus-inert" PEG and facilitate epithelial cell endocytosis via specific interaction between butyrate and monocarboxylate transport 1 (MCT1), thus ameliorating intestinal absorption into blood circulation.[16] More importantly, MCT-1 is not only differentially expressed on the apical and basolateral sides of intestine, but also highly expressed on the surface of malignant HCC cells in comparison with normal hepatocytes.[17,18] Moreover, we recently reported that poly (lactic-co-glycolic acid) (PLGA)-lipid nanoparticles mainly accumulated in the liver after oral administration.[19]

Y. Yu, X. Shen, X. Xiao, L. Li, Y. Huang
Key Laboratory of Drug-Targeting and Drug Delivery System of the Education Ministry and Sichuan Province
Sichuan Engineering Laboratory for Plant-Sourced Drug and Sichuan Research Center for Drug Precision Industrial Technology
West China School of Pharmacy
Sichuan University
Chengdu 610041, P. R. China
E-mail: huangyuan0@163.com

The ORCID identification number(s) for the author(s) of this article can be found under https://doi.org/10.1002/smll.202301149

**DOI: 10.1002/smll.202301149**

 

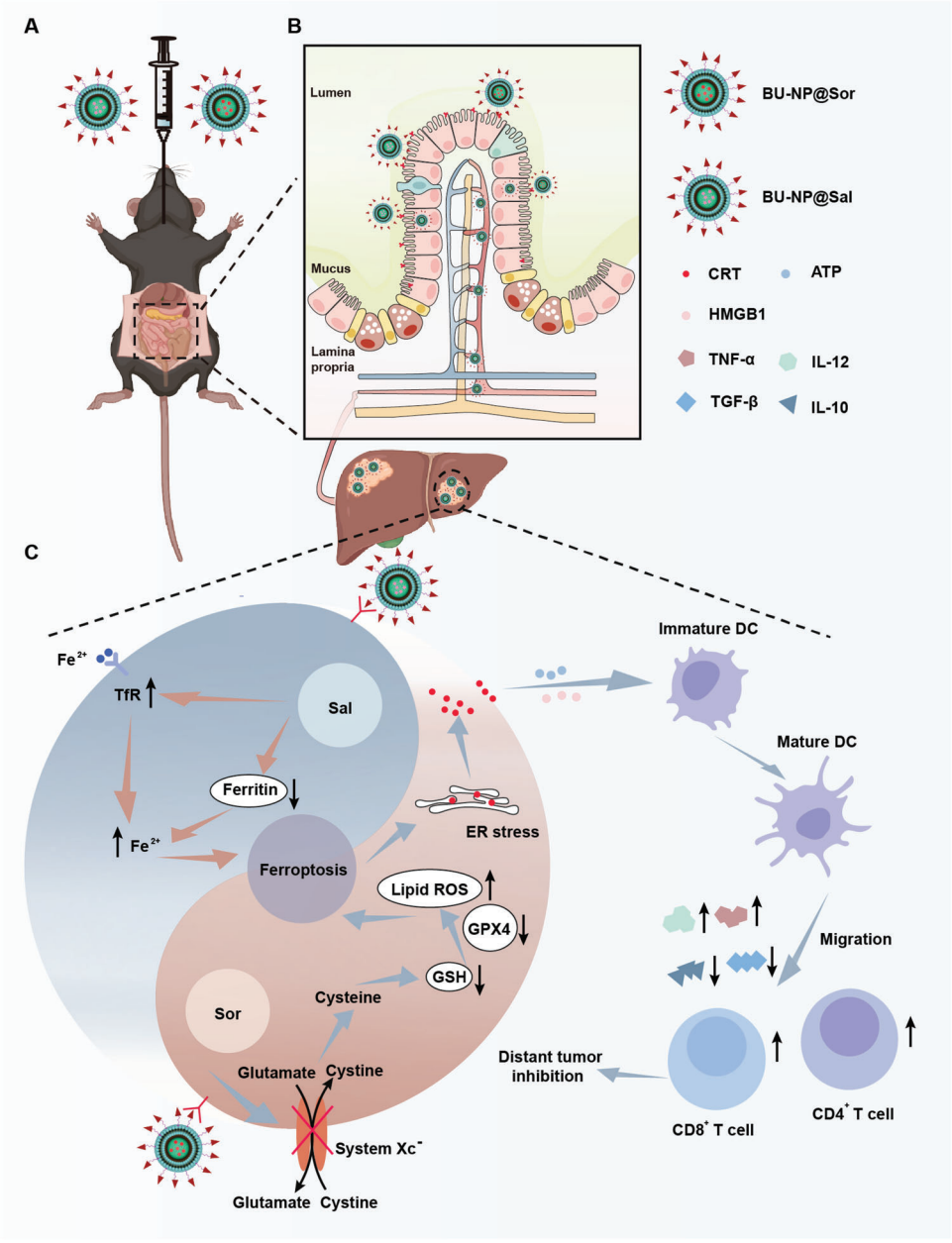


**Scheme 1.** Schematic illustration of the combination therapy (BU-NP@Sor/Sal). A) Orthotopic HCC-bearing mice were orally administered with BU-NP@Sor/Sal. B) Butyrate modification enhanced oral absorption and tumor accumulation of nanoparticles. C) BU-NP@Sor/Sal treatment induced ferroptosis and ICD, improving the anti-tumor effect.

Hence, butyrate-functionalized PLGA-lipid nanoparticles might transport intestinal epithelium into blood circulation, distribute in the liver, and deliver medicines to hepatoma cells via MCT-1-mediated endocytosis.

In this work, we prepared butyrate-modified PLGA-lipid nanoparticles to target intestinal epithelium and liver cancer cells (**Scheme 1**). To improve the anti-tumor effect of Sor, another ferroptosis inducer salinomycin (Sal) was adopted in combination with Sor. Sal could increase the level of iron-responsive element-binding protein 2 (IRP2) , promote the level of transferrin receptor (TfR), and reduce the level of ferritin (Fer), thereby augmenting cellular iron concentration.[20–22] In this regard, combining Sor and Sal might be feasible for effective ferroptosis therapy. As a proof of concept, Sor and Sal were separately loaded into nanoparticles for synergistic HCC therapy by inducing ferroptosis and immune activation. We demonstrated that Sor-induced lipid peroxides and Sal further augmented iron ions by promoting the level of TfR and reducing the level of Fer. Notably, the reactive oxygen species (ROS) upregulation during ferroptosis also led to endoplasmic reticulum (ER) stress, thus enhancing the calreticulin (CRT) exposure for increasing the immunogenic cell death (ICD). Moreover, combination nanoparticles exerted a satisfactory anti-HCC effect in vivo. These findings provide an effective oral delivery strategy for ferroptosis inducers against HCC.

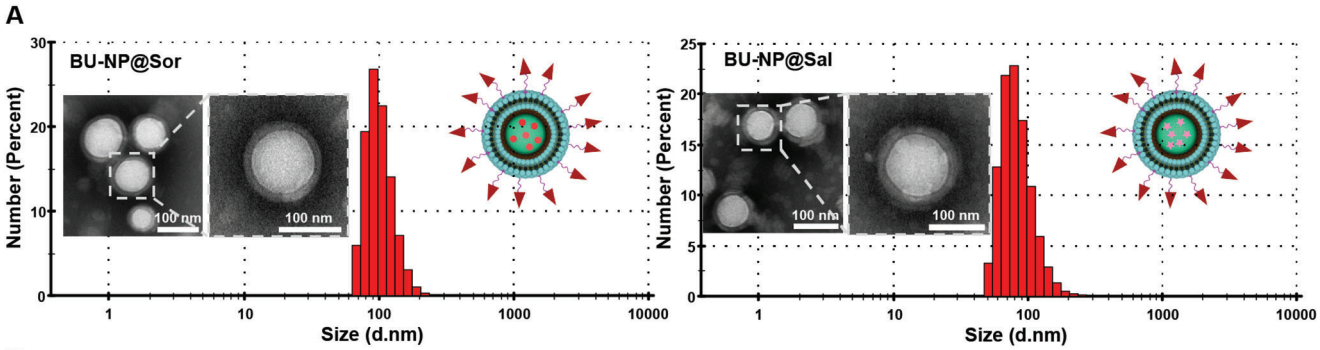


B

| Samples | Size (nm) | PDI | Zeta potential (mV) | Encapsulation efficiency (%) | Drug loading (%) |
|---|---|---|---|---|---|
| BU-NP@Sor | 138.1 ± 1.36 | 0.261 ± 0.024 | -23.2 ± 0.94 | 71.46 ± 2.33 | 2.15 ± 0.16 |
| BU-NP@Sal | 125.5 ± 3.26 | 0.195 ± 0.033 | -24.6 ± 5.91 | 57.69 ± 5.67 | 1.64 ± 0.16 |

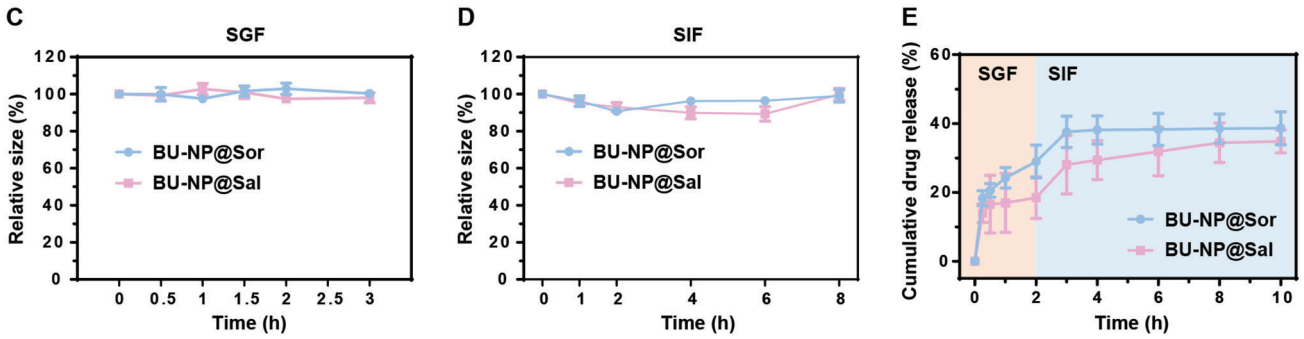


**Figure 1.** Characterization of nanoparticles. A) Size distribution and transmission electron microscopy images (inserts) of BU-NP@Sor and BU-NP@Sal. B) Characterizations of butyrate-modified drug-loaded nanoparticles. The hydrodynamic size changes in simulated gastric fluid (C) and simulated intestinal fluid (D). E) Drug release profiles in simulated physiological media. Mean ± SD, $n = 3$.

## 2. Results and Discussion

### 2.1. Preparation and Characterization of Nanoparticles

Sor-loaded nanoparticles (BU-NP@Sor) and Sal-loaded nanoparticles (BU-NP@Sal) with butyrate modification (Figure S1, Supporting Information) were prepared via a two-step approach according to our previous study.[23] Both nanoparticles were spherical, as observed by transmission electron microscopy (TEM), with diameters ≈130 nm and were ≈−20 mV in zeta potential (**Figure 1**A,B). The encapsulation efficiency of BU-NP@Sor and BU-NP@Sal was 71.46% ± 2.33% and 57.69% ± 5.67%, with the drug loading of 2.15% ± 0.16% and 1.64% ± 0.16%, respectively (Figure S2, Supporting Information). Stability tests showed that the hydrodynamic sizes of both nanoparticles underwent no obvious variations in simulated gastric fluid (SGF, Figure 1C) and simulated intestinal fluid (SIF, Figure 1D). Moreover, the cumulative release of Sor and Sal was <40% in simulated gastroenteric media within 10 h (Figure 1E). Overall, these results demonstrated that BU-NP@Sor and BU-NP@Sal had good physiological stability that meets the prerequisites for oral administration.[24]

### 2.2. Butyrate-Functionalization Facilitates Cellular Uptake and Permeability In Vitro

The expression of the receptors is the first prerequisite for receptor-mediated endocytosis.[25] Both immunofluorescence staining (Figure S3, Supporting Information) and western blot (**Figure 2**A) results confirmed substantial MCT-1 expression on human colon adenocarcinoma (Caco-2) cells and mouse hepatoma (Hepa1-6) cells but barely on normal human liver (LO2) cells. Then, Caco-2 cells, Hepa1-6 cells, and LO2 cells were incubated with coumarin (C6)-loaded nanoparticles without butyrate modification (PEG-NP@C6) and with butyrate functionalization (BU-NP@C6), respectively, and then quantitatively compared to cellular uptake (Figure 2B–D). Results showed that the uptake of BU-NP@C6 was significantly higher ($p<0.001$) than PEG-NP@C6 in Caco-2 cells and Hepa1-6 cells, whereas no significant

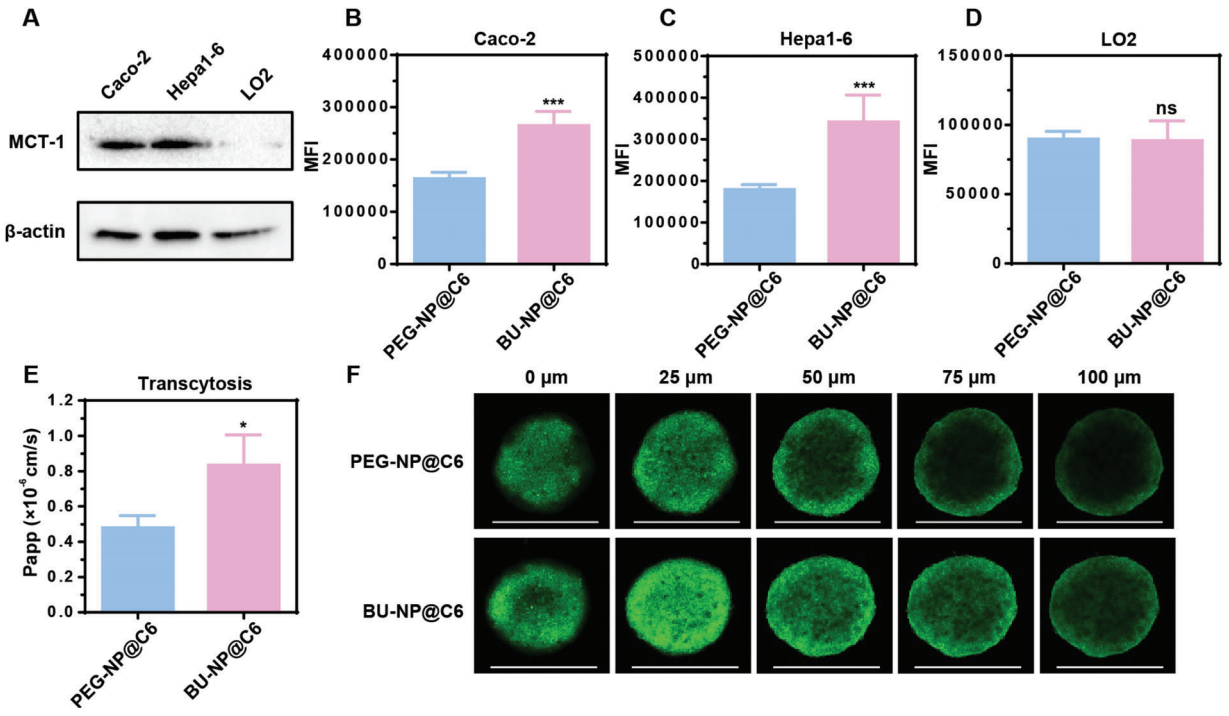


**Figure 2.** Cellular uptake and permeability of nanoparticles. A) Western blotting analyses of MCT-1 in human intestinal epithelial (Caco-2) cells, mouse hepatoma (Hepa1-6) cells, and normal human liver (LO2) cells. The mean fluorescent intensities (MFI) of C6 within Caco-2 cells (B), Hepa1-6 cells (C), and LO2 cells (D). Mean ± SD, $n = 3$. *** $p<0.001$, ns $p>0.05$. E) The apparent permeability coefficient (Papp) during transport across Caco-2 cells. Mean ± SD, $n = 3$. * $p<0.05$. F) Hepa1-6 multicellular tumor spheroids infiltration of the C6-loaded nanoparticles. Scale bar: 500 μm.

difference ($p>0.05$) was observed in LO2 cells. Additionally, the mechanism of the endocytic pathway was explored (Figure S4, Supporting Information). MCT-1 inhibitor sodium butyrate significantly reduced the cellular uptake of BU-NP@C6 in Caco-2 and Hepa1-6 cells, but not PEG-NP@C6 or in LO2 cells, indicating that the uptake of BU-NP@C6 was related to MCT-1 mediated endocytosis in Caco-2 and Hepa1-6 cells.

Subsequently, the in vitro transepithelial transport was evaluated on the Caco-2 cell monolayer. Like the observations in cellular uptake assays, BU-NP@C6 had an increased apparent permeability coefficient (Papp) compared to PEG-NP@C6 (Figure 2E). In addition, the tumor infiltration was assessed using Hepa1-6 multicellular tumor spheroids (Figure 2F). Of note, BU-NP@C6 had bright fluorescence in the Hepa1-6 cellular spheroid surface and interior after incubation 3 h, while the spheroid incubated with PEG-NP@C6 confined the fluorescence at the outer layers, indicating that BU-NP@C6 induced efficient penetration in Hepa1-6 multicellular tumor spheroids.

Collectively, our results demonstrated that butyrate-functionalization facilitated endocytosis and permeability of BU-NP@C6 in MCT-1-positive Caco-2 cells and Hepa1-6 cells.

### 2.3. Butyrate Modification Enhances In Vivo Absorption and Tissue Accumulation

Next, in vivo oral absorption of nanoparticles was evaluated. First, in situ absorption in the rat intestine was observed by a confocal laser scanning microscope (CLSM, **Figure 3**A). BU-NP@C6 exhibited higher green fluorescence than PEG-NP@C6 in intestinal villi, suggesting enhanced intestinal absorption. Similar findings were also observed in the ex vivo intestinal loop model (Figure 3B). BU-NP@C6 showed a higher Papp value permeating through the intestinal loop than PEG-NP@C6. These results correlated with the favorable pharmacokinetic behavior of BU-NP@C6, as shown in Figure 3C and Table S1 (Supporting Information). The area under the curve ($AUC_{0\text{-}12\,h}$) and maximum concentration ($C_{max}$) of the orally administered BU-NP@C6 was 68.81 μg*h/mL and 11.04 μg $mL^{-1}$, respectively. These values were significantly higher than those for PEG-NP@C6 (58.02 μg*h/mL and 7.82 μg $mL^{-1}$).

We further investigated the in vivo distribution of DiR-loaded nanoparticles in mice bearing Hepa1-6 orthotopic tumors. As shown in Figure 3D, the mice orally administered with BU-NP@DiR had strong fluorescence in their middle abdomens. The fluorescence intensity decreased with time but remained strong at 6 h and was visible after 12 h, while the fluorescence was weaker after 12 h in the orally administered free DiR group. Moreover, ex vivo imaging demonstrated that after BU-NP@DiR treatment, the main absorption sites of the gastrointestinal tract-the duodenum, jejunum, ileum, and cecocolon, had stronger fluorescence than that with PEG-NP@DiR or free DiR (Figure S5, Supporting Information). Accordingly, at 12 h post-administration, the liver fluorescence intensity in the BU-NP@DiR-treated mice was significantly higher than that of PEG-NP@DiR and free DiR (Figure 3E). More importantly, with the aid of butyrate targeting on the MCT-1 receptor, most

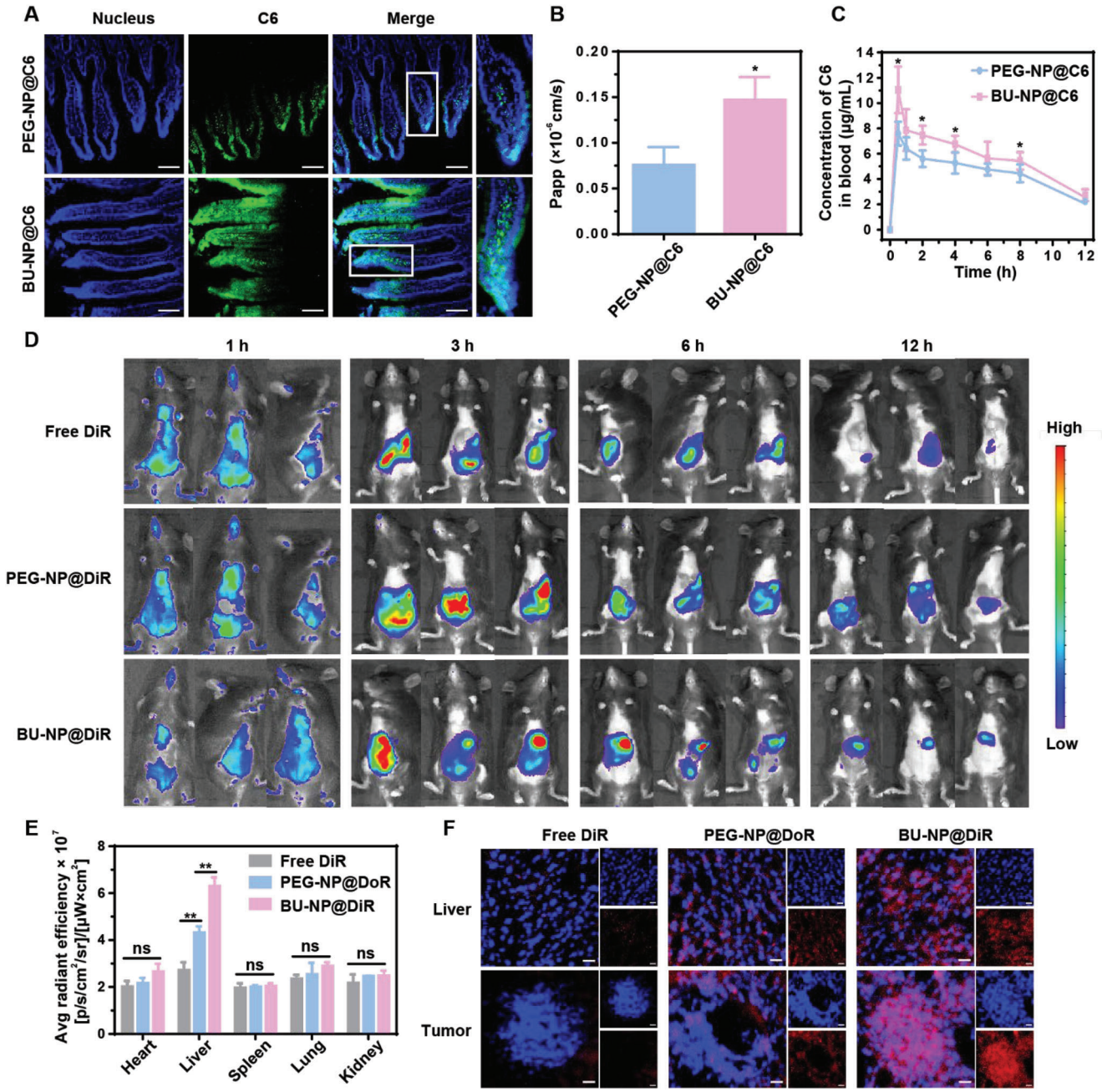


**Figure 3.** The oral absorption and distribution of nanoparticles in vivo. A) Representative fluorescence images of rats' intestines post-administration with C6-loaded nanoparticles. The boxed areas are enlarged at the right panel. Scale bar: 100 μm. B) The Papp value of C6-loaded nanoparticles penetrating through ex vivo intestinal sections. Mean ± SD, $n = 3$. * $p<0.05$. C) Plasma concentration of C6 after mice oral administration of C6-loaded nanoparticles. Mean ± SD, $n = 5$. * $p<0.05$, versus PEG-NP@C6. D) In vivo fluorescence imaging of C57 mice after timed intervals of oral administration of free DiR or DiR-loaded nanoparticles. E) The quantification of the fluorescence in the heart, liver, spleen, lungs, and kidneys. Mean ± SD, $n = 3$. ns $p>0.05$, ** $p<0.01$. F) Fluorescence imaging detected DiR in normal liver and tumor tissue. Red: DiR; blue: cell nucleus. Scale bar: 20 μm.

nanoparticles were taken up by tumor cells in the liver, which could be verified by CLSM images after 12 h of oral administration (Figure 3F; Figure S6, Supporting Information).

Taken together, our results revealed that butyrate modification could enhance oral absorption and hepatic tumor accumulation.

### 2.4. Combination of BU-NP@Sor and BU-NP@Sal Synergistically Induces Ferroptosis and Immunogenic Cells Death In Vitro

To evaluate Sor and Sal's in vitro synergistic effect, we first examined the cytotoxicity of the combination in different molar ratios after treatment in Hepa1-6 cells (Figure S7, Supporting

Information). When the molar ratio of Sor and Sal was 1:10, the CI<1 over various drug concentrations was observed, indicating the synergy.[26] More impressively, both targeted nanoparticle combinations (BU-NP@Sor/Sal) exhibited much higher cytotoxicity than monotherapy BU-NP@Sor and BU-NP@Sal, which might be attributed to the synergistic effect of Sor and Sal (**Figure 4**A). Furthermore, BU-NP@Sor/Sal displayed enhanced cytotoxicity than PEG-NP@Sor/Sal, which was attributed to the butyrate-mediated targeting to enable increased endocytosis of the nanoparticles (Figure 4A; Figure S8, Supporting Information). In contrast, the viability of LO2 cells after treatment with BU-NP@Sor/Sal and PEG-NP@Sor/Sal was comparable with no significant difference (Figure S9, Supporting Information), suggesting that butyrate modification did not induce enhanced cytotoxicity in normal liver cells.

To make clear the cell death mechanism, we first evaluated whether the ferrostatin-1 (Fer-1, a ferroptosis inhibitor) could relieve the cytotoxicity.[27,28] As shown in Figure 4B, Fer-1 could significantly alleviate the cytotoxicity of BU-NP@Sor/Sal. Meanwhile, the presence of deferoxamine (DFO, an iron-chelating agent) could also improve cell viability (Figure S10, Supporting Information). Overall, these results suggested that ferroptosis was probably responsible for the BU-NP@Sor/Sal-induced cell death.

As reported, Sor is the system $X_c^-$ inhibitor that mediates the transportation of cystine into cells and generates cysteine.[12] This inhibition prevents new glutathione (GSH) synthesis and causes GPX4 down-regulation and the generation of lipid peroxidation, leading to ferroptosis.[12] As illustrated in Figure 4C, BU-NP@Sor/Sal treatment enhanced cellular GSH depletion more dramatically than the controls (including free Sor/Sal, PEG-NP@Sor/Sal, BU-NP@Sor, and BU-NP@Sal) did. Furthermore, BU-NP@Sor/Sal treatment more effectively resulted in the down-regulation of GPX4 in Hepa1-6 cells (Figure 4D; Figure S11, Supporting Information). Additionally, Sal can improve intracellular iron by increasing IRP2 and TfR, and rapidly degrading Fer (an iron storage protein).[20,29] Western blot analysis indicated that treatment of Hepa1-6 cells with BU-NP@Sor/Sal increased the level of TfR along with the decreased level of Fer (Figure 4D). Figure 4E,F confirmed that combined treatment with BU-NP@Sor/Sal significantly increased ROS and lipid peroxidation malondialdehyde (MDA) levels more effectively than treatment with BU-NP@Sor or BU-NP@Sal alone ($p<0.05$). Moreover, TEM images of BU-NP@Sor/Sal treated Hepa1-6 cells showed apparent mitochondria shrinkage, a feature of ferroptosis-induced mitochondrial dysfunction (Figure 4G).[30,31]

zPrevious reports suggested that ferroptosis is able to induce ICD for immune activation.[32] Of note, the BU-NP@Sor/Sal treatment caused the up-regulation of human endoplasmic reticulum stress-related proteinCHOP (Figure 4H), reflecting the appearance of ER stress in tumor cells.[33] Furthermore, the BU-NP@Sor/Sal group exhibited higher exposure of CRT than BU-NP@Sor and BU-NP@Sal ($p<0.001$, Figure 4I), suggesting that the combination of Sor and Sal caused a higher degree of ICD than single-mode treatment. Similarly, the BU-NP@Sor/Sal treatment exhibited the most significant release of adenosine triphosphate (ATP) among all groups owing to the butyrate-promoted cellular uptake ($p<0.05$, Figure 4J). Meanwhile, the release of high mobility group box 1 protein (HMGB1) induced by BU-NP@Sor/Sal was significantly higher than that in other groups ($p<0.05$, Figure 4Q), illustrating that the best ICD effect could be induced by the BU-NP@Sor/Sal nano-complexes through enhanced ferroptosis.

Above all, these results demonstrated that BU-NP@Sor/Sal could enhance ferroptosis and immunogenic cells death by utilizing the advantageous combination of BU-NP@Sor and BU-NP@Sal: 1) BU-NP@Sor induced ferroptosis by down-regulation GPX4 and generation lipid peroxidation; 2) BU-NP@Sal further amplified ferroptosis via increased intracellular iron.

### 2.5. Combination of BU-NP@Sor and BU-NP@Sal Synergistically Induces Ferroptosis to Suppress HCC Development

To validate the effect of BU-NP@Sor/Sal in vivo, Hepa1-6-Luc cells were injected into mice's livers to establish the HCC model. Three days after inoculation, intragastric administration with nanoparticles was performed every other day for a continuous five times (**Figure 5**A). Notably, BU-NP@Sor/Sal markedly inhibited rapid tumor growth compared to the distilled water group, while either BU-NP@Sor or BU-NP@Sal exhibited a weak effect (Figure 5B,C). In addition, BU-NP@Sor/Sal exerted higher efficacy than free Sor/Sal and PEG-NP@Sor/Sal. Particularly, an impressive survival prolongation was observed from 32 d in the distilled water group to 70 d in the BU-NP@Sor/Sal group (Figure 5D). The liver with tumors was excised on day 21, and the luciferase intensity in BU-NP@Sor/Sal group was significantly lower than that in other groups (Figure 5E). Moreover, BU-NP@Sor/Sal with targeted butyrate exhibited a more obvious effect than PEG-NP@Sor/Sal without the target. Besides, GSH depletion (Figure 5F), GPX4 downregulation (Figure 5G), TfR upregulation, Fer degradation, lipid ROS (Figure 5H), and MDA upregulation (Figure 5I) were observed in the tumor, confirming the in vivo ferroptosis induced by BU-NP@Sor/Sal. Thus, BU-NP@Sor and BU-NP@Sal synergistically induced ferroptosis to suppress HCC development.

### 2.6. Combination of BU-NP@Sor and BU-NP@Sal Synergistically Activates Immunity

To further confirm whether the combination of BU-NP@Sor and BU-NP@Sal could induce the ICD effect in vivo, the markers CRT, ATP, and HMGB1 were examined 3 days after therapy. In consistence with the in vitro results, combination treatment with BU-NP@Sor and BU-NP@Sal resulted in the highest CRT exposure (**Figure 6**A), ATP (Figure 6B), and HMGB1 release (Figure 6C) indicative of further promoted ICD induction. Interestingly, BU-NP@Sor/Sal (0.319%) treatment presented markedly higher $CD8^+$ T cells than distilled water (0.014%), free Sor/Sal (0.142%), PEG-NP@Sor/Sal (0.217%), BU-NP@Sor (0.085%), and BU-NP@Sal (0.063%) (Figure 6D). BU-NP@Sor/Sal also induced the highest percentage of $CD4^+$ T cells (Figure S12, Supporting Information) and activated DC cells (Figure 6E). Comparatively, either BU-NP@Sor or BU-NP@Sal displayed a partial effect on immune cells. Accordingly, BU-NP@Sor/Sal therapy significantly boosted the release

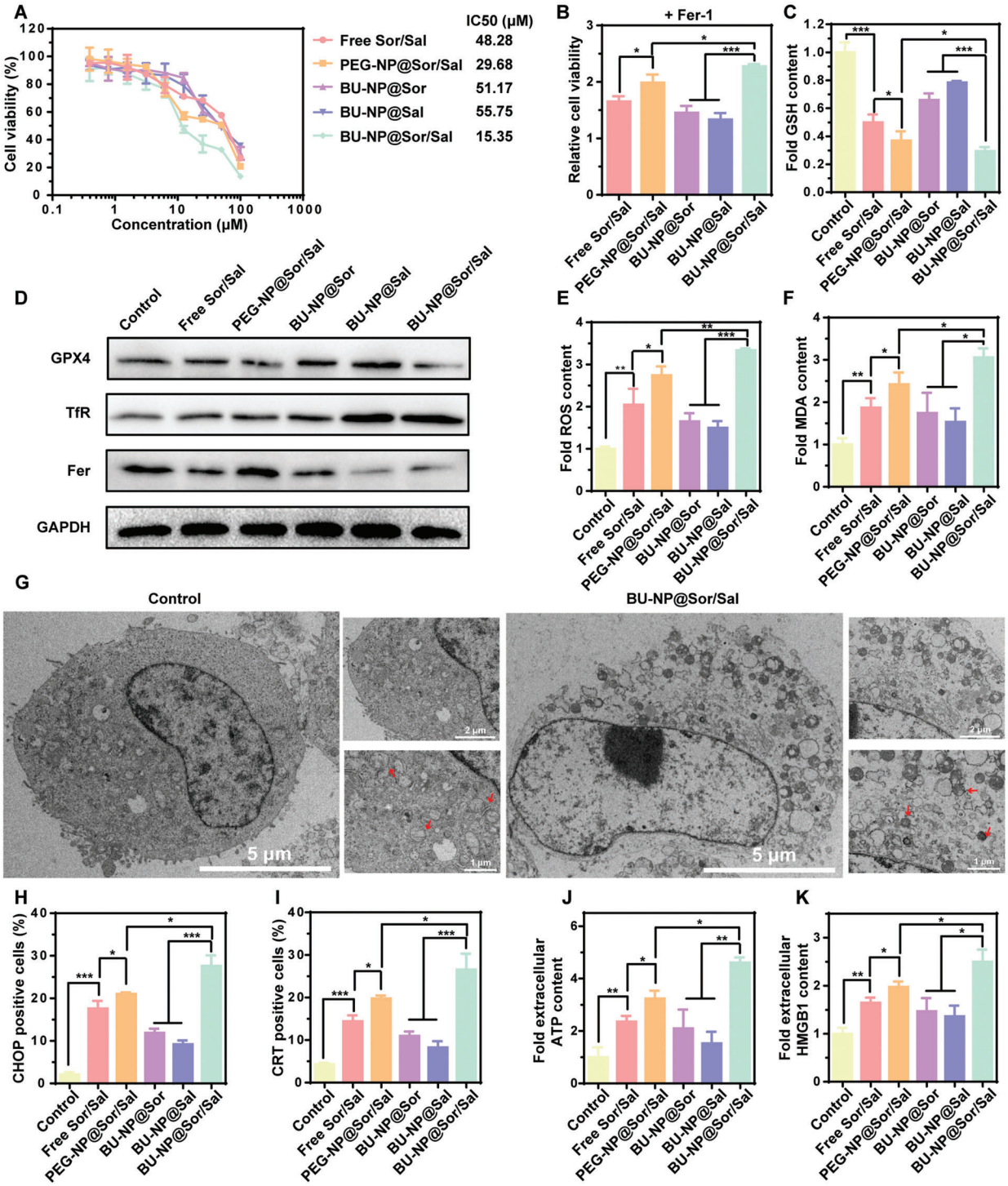


**Figure 4.** The combination of BU-NP@Sor and BU-NP@Sal synergistically induced ferroptosis and immunogenic cell death in vitro. A) Hepa1-6 cells cytotoxicity study. Mean ± SD, $n = 3$. B) Relative cell viability of free Sor/Sal, PEG-NP@Sor/Sal, BU-NP@Sor, BU-NP@Sal, or BU-NP@Sor/Sal treated Hepa1-6 cells after the addition of Fer-1. * $p<0.05$, *** $p<0.001$. Mean ± SD, $n = 3$. C) Intracellular GSH level of Hepa1-6 cells after treatment with free Sor/Sal, PEG-NP@Sor/Sal, BU-NP@Sor, BU-NP@Sal, and BU-NP@Sor/Sal with an equivalent Sor dosage at 10 μM. * $p<0.05$, *** $p<0.001$. Mean ± SD, $n = 3$. D) Western blot analysis of GPX4, TfR, and Fer expression in Hepa1-6 cells. E) Intracellular ROS level. * $p<0.05$, ** $p<0.01$, *** $p<0.001$. Mean ± SD, $n = 3$. F) Intracellular MDA content. * $p<0.05$, ** $p<0.01$. Mean ± SD, $n = 3$. G) Mitochondrial morphological images of Hepa1-6 cells were observed by TEM. The red arrows indicate the mitochondria. H) Flow cytometry analysis of CHOP positive cells after incubation with free Sor/Sal, PEG-NP@Sor/Sal, BU-NP@Sor, BU-NP@Sal, and BU-NP@Sor/Sal, respectively. * $p<0.05$, *** $p<0.001$. Mean ± SD, $n = 3$. I) CRT exposure of Hepa1-6 cells. * $p<0.05$, *** $p<0.001$. Mean ± SD, $n = 3$. J) The ratio of extracellular ATP. * $p<0.05$, ** $p<0.01$. Mean ± SD, $n = 3$. K) HMGB1 level was detected by the ELISA kit. * $p<0.05$, ** $p<0.01$. Mean ± SD, $n = 3$.

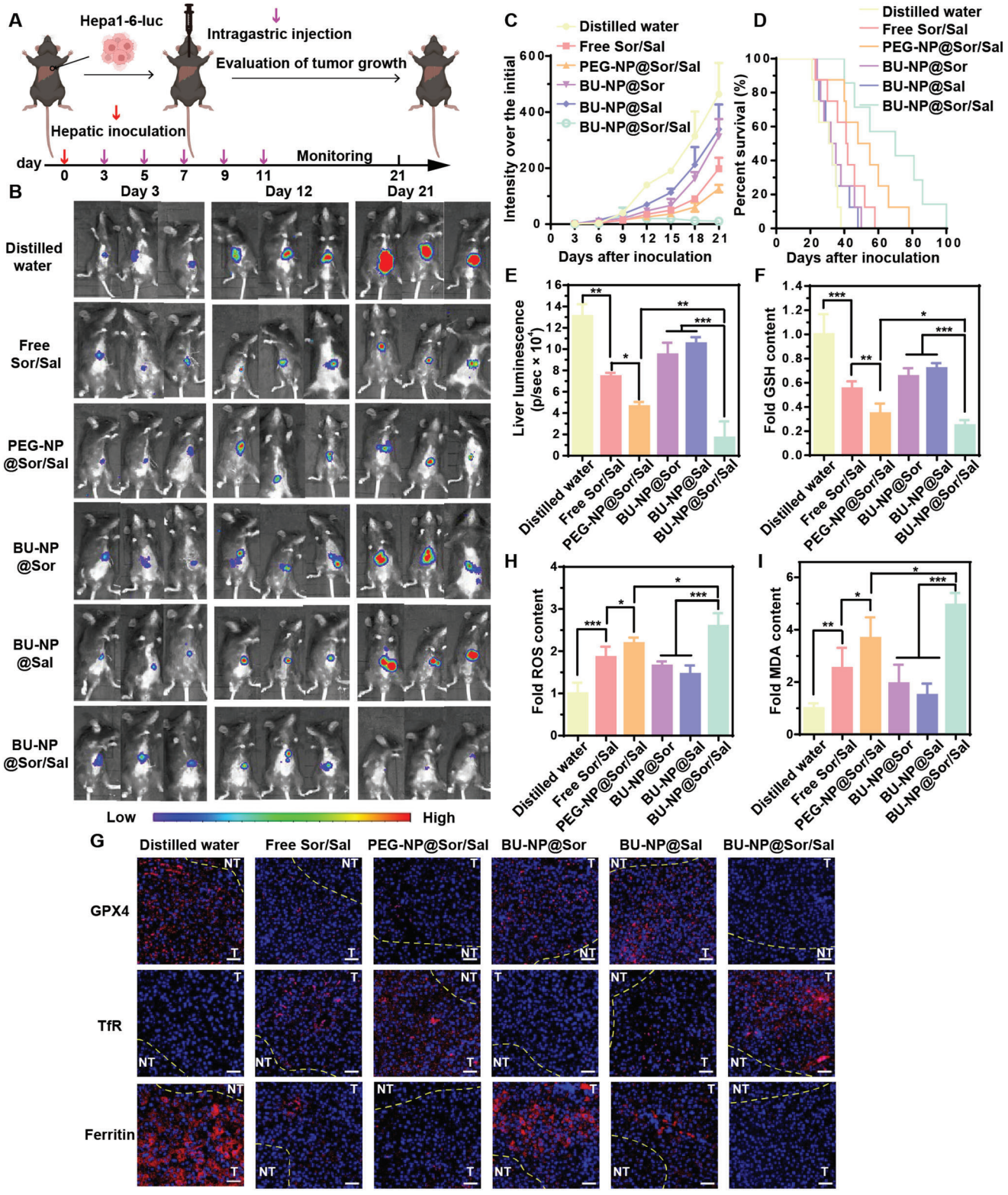


**Figure 5.** Combo nanoparticles suppress hepatocarcinoma development. A) Scheme of tumor inoculation and treatment. B) Bioluminescence images, C) tumor growth curves, and D) survival curves of Hepa1-6 tumor-bearing mice in different treatment groups. E) Quantification of hepatic tumor luciferase at day 21 after inoculation. F) The GSH level in the tumor. G) Immunofluorescence images of GPX4, TfR, and Fer in the liver. Red: indicates GPX4, TfR, and Fer; blue: indicates DAPI (nucleus). Scale bar: 50 μm. Lipid ROS H) and MDA I) levels in the tumor. * $p<0.05$, ** $p<0.01$, *** $p<0.001$, mean ± SD ($n = 5$).

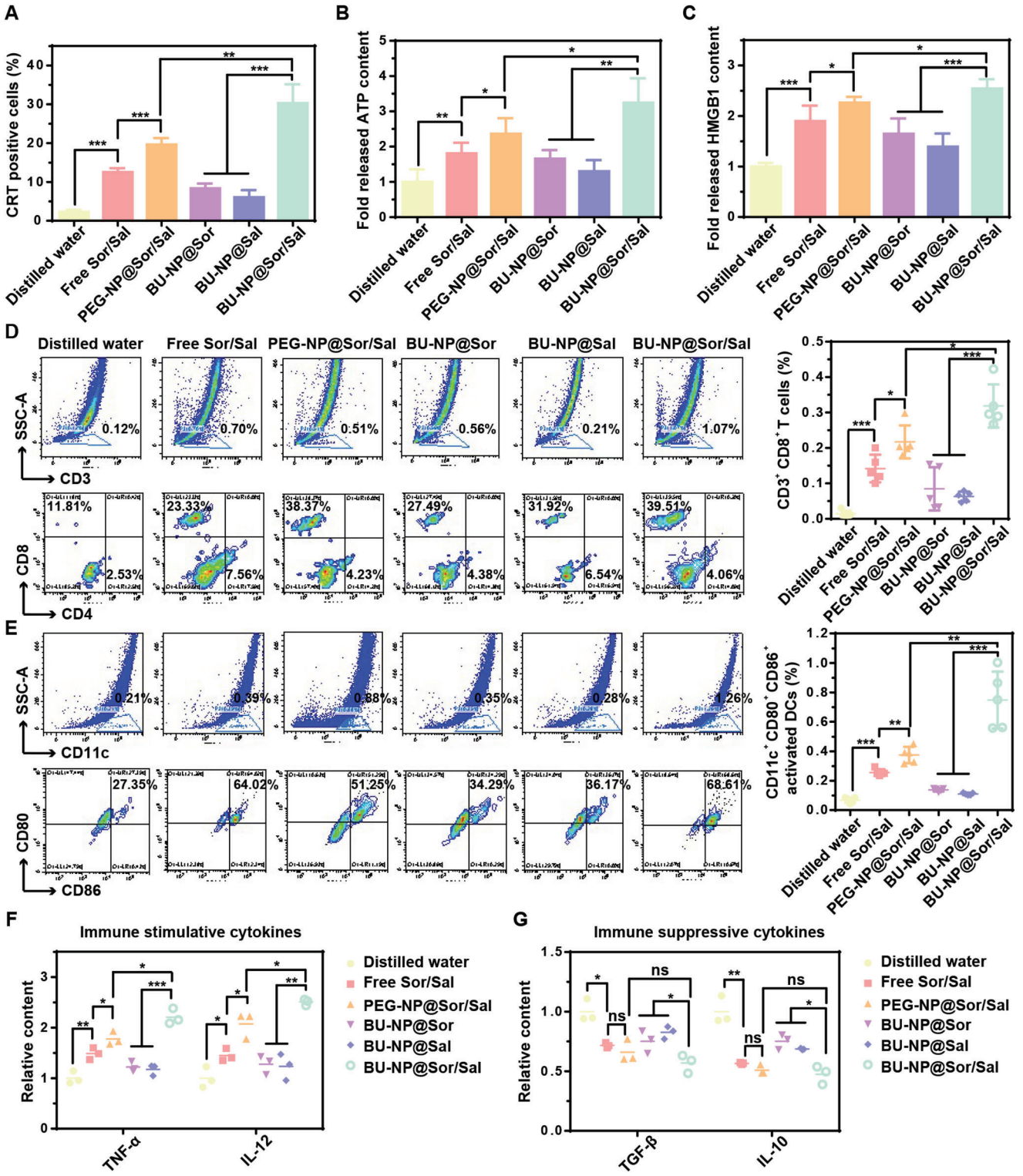


**Figure 6.** Combo nanoparticles remodel the immune microenvironment. A) CRT-positive cells. ATP (B) and HMGB1 (C) levels. D) The infiltration of $CD8^+$ T cells was detected by flow cytometry. E) The activated DCs. The immune stimulate cytokines (F) and immune-suppressive cytokines (G) were detected by ELISA kits. * $p<0.05$, ** $p<0.01$, *** $p<0.001$, mean ± SD ($n = 5$).

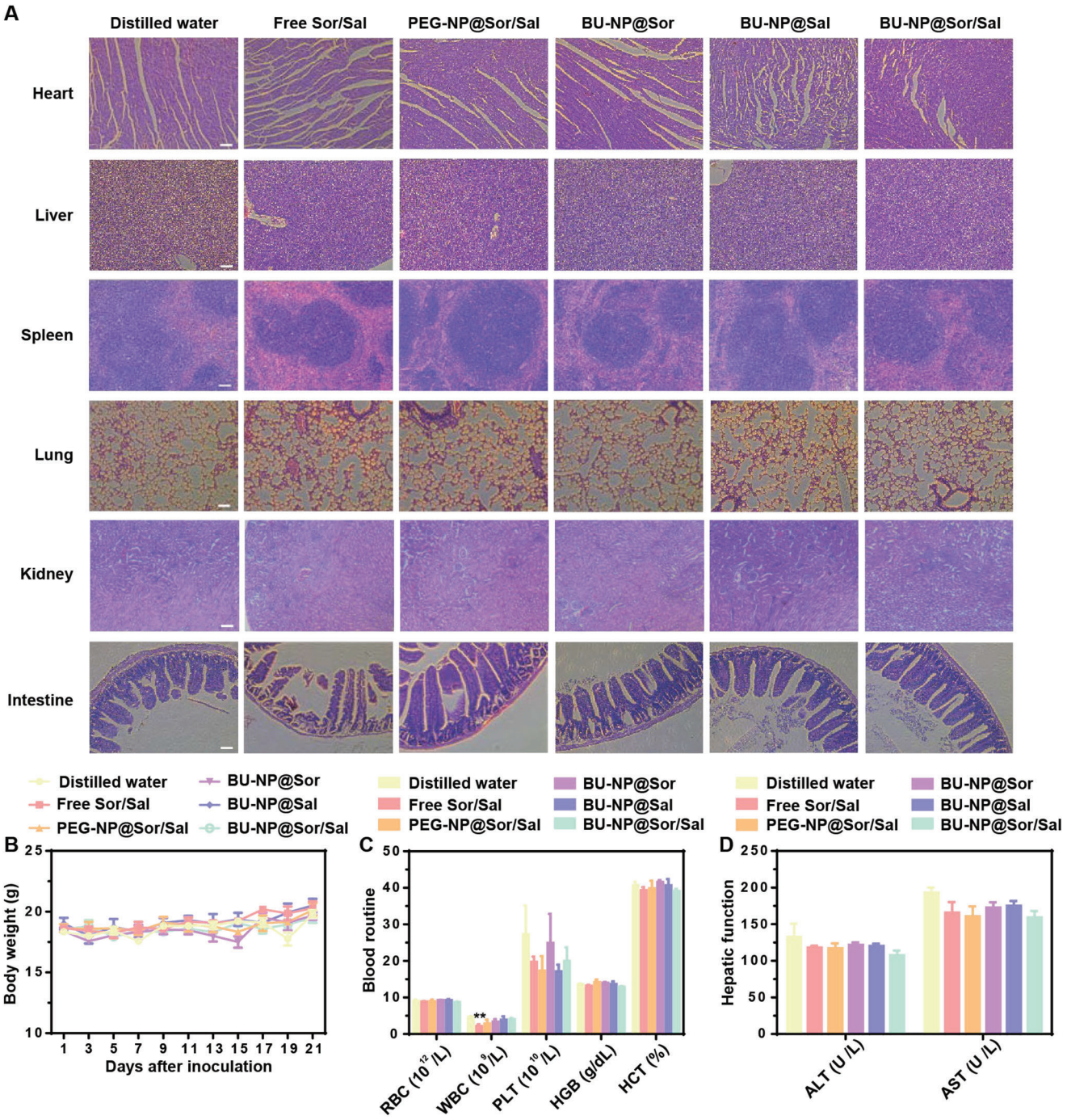


**Figure 7.** The combination of nanoparticles showed no obvious toxicity. A) H&E staining of major organs from mice in different therapy groups. Scale bar: 100 μm. B) Mice's body weight changes. Mean ± SD ($n$ = 5). C) Mice's blood routine test. Mean ± SD ($n$ = 5). ** $p$<0.01 versus distilled water group. D) Mice hepatic function test. Mean ± SD ($n$ = 5).

of immunostimulatory cytokines TNF-$\alpha$ and IL-12 (Figure 6F), while decreasing immunosuppressive cytokines TGF-$\beta$ and IL-10 (Figure 6G). Taken together, the combination of BU-NP@Sor and BU-NP@Sal synergistically enhanced anti-tumor immunity.

### 2.7. Oral Administration of Nanoplatforms Shows Considerable Biocompatibility

To assess the safety of nanoparticles for oral administration, we conducted the assessment of biosafety-associated histopathology

and hematology. Hematoxylin and eosin (H&E) staining demonstrated no significant erosion in main organs, including the heart, liver, spleen, lung, kidney, and intestine, after treatment of distilled water and nanoparticles pharmacy (**Figure 7**A). Conversely, the muscularis mucosa of the intestine was destroyed in the free Sor/Sal group. Meanwhile, the mice's body weight showed no noticeable loss during the experiment (Figure 7B). Among multiple hematological parameters, a decrease in white blood cells was observed in the free Sor/Sal group, while not observed in the nanoparticle groups (Figure 7C). In addition, the hepatic function test further confirmed the considerable biocompatibility of the nanoformulations (Figure 7D). Taken together, these results suggested that our nano-delivery system had outstanding biological safety for oral anti-liver cancer.

### 2.8. BU-NP@Sor Together with BU-NP@Sal Exert an Anti-Tumor Vaccination Effect and Achieve the Synergistic Effect in Late-Stage HCC

The critical characteristic of ICD is its ability to mediate the antitumor vaccine effect. To further evaluate whether the combination therapy of BU-NP@Sor and BU-NP@Sal could induce an anticancer memory effect, orthotopic HCC-bearing mice treated with the BU-NP@Sor/Sal were rechallenged by subcutaneous inoculation of Hepa1-6-Luc cells and analyzed after 16 days (**Figure 8**A). Strikingly, in BU-NP@Sor/Sal group, barely tumors were observed, while tumors grew rapidly in the naïve group (Figure 8B; Figure S13, Supporting Information). In addition, the BU-NP@Sor/Sal treated mice had significantly higher frequencies of $CD8^+$ T cells and memory effector $CD8^+$ T cells in peripheral blood and spleen than the naïve group (Figure 8C,D), indicating the establishment of potent immune memory response against cancer recurrence.

In the clinic, HCC is always detected at an advanced stage. To investigate whether the combination treatment of BU-NP@Sor and BU-NP@Sal could exert a suppressive effect in advanced HCC, we started the therapy 10 days after orthotopic inoculation (Figure 8E). As expected, the prognosis of cancer in the advanced stage is much worse than in the early stage, whereas BU-NP@Sor/Sal still achieved a significant therapeutic effect than control (Figure 8F,G).

Taken together, the combination therapy of BU-NP@Sor and BU-NP@Sal exerted strong immune surveillance in tumor recurrence and achieved therapeutic effects in the advanced HCC.

## 3. Conclusion

To summarize, we constructed an oral delivery platform to target and suppress hepatic cancer. Our results validated that butyrate modification enabled higher intestinal absorption and tumor accumulation of BU-NP@Sor/Sal. Furthermore, BU-NP@Sor might cause ferroptosis in the tumor by depleting GSH, downregulating GPX4, and increasing lipid peroxidation. In addition, BU-NP@Sal amplified the ferroptosis by increasing iron ions concentration. Moreover, the combined treatment of BU-NP@Sor and BU-NP@Sal triggered a robust immune effect and induced a strong immune memory response. Accordingly, this combinatory nanoplatform exerted satisfactory anti-HCC effects both at an early and advanced stage.

## 4. Experimental Section

*MTT Assay*: To measure the cytotoxicity, Hepa1-6 or LO2 cells were seeded into 96-well plates and cultured for 24 h. The cells were incubated with different drugs for 24 h, then each well was added with 15 µL medium containing 5 mg $mL^{-1}$ MTT for another 4 h incubation. The medium in each well was discarded and replaced with 150 µL DMSO to dissolve the formazan crystals. The absorbance was detected at 490 nm using a microplate reader (Varioskan LUX, Thermo Fisher Scientific, Massachusetts, USA), and the cell viability was calculated.

*Cellular GSH Assay*: The Hepa1-6 cells were seeded into 12-well plates and cultured for 24 h. After various treatments, the cells were washed with PBS and harvested. Next, the cells were treated with the protein removal reagent and lysed by repeated freezing and thawing. After that, the samples were collected by centrifugation and mixed with DTNB work solution and NADPH solution. After 30 min of co-incubation, the absorbance was detected at 412 nm using a microplate reader.

*Cellular ROS Assessment*: The Hepa1-6 cells were seeded into 12-well plates and cultured for 24 h. After various treatments, the cells were harvested and washed with PBS. Next, the cells were collected by centrifugation and treated with DCFH-DA. After 20 min of co-incubation, the cells were washed with PBS, and the fluorescence intensity was detected by flow cytometry.

*Cellular MDA Assay*: The Hepa1-6 cells were seeded into 12-well plates and cultured for 24 h. After various treatments, the cells were harvested and washed with PBS. Next, the cells were lysed with RIPA lysis buffer. After that, the lysis buffer was mixed with the MDA work solution. After 15 min of co-incubation in boiling water, the samples were collected by centrifugation and measured at 532 nm using a microplate reader.

*In Vitro GPX4, TfR, and Fer Analysis by Western Blot*: The Hepa1-6 cells were seeded in the 6-well plates and cultured for 24 h. After various treatments, the cells were washed with PBS and lysed with RIPA lysis buffer. Next, the samples were harvested by centrifugation and mixed with SDS-PAGE protein staining and loading buffer. After 10 min of co-incubation in boiling water, the GPX4, TfR, and Fer expression levels were measured using electrophoresis.

*Mitochondrion Observation*: The Hepa1-6 cells were cultured in cell-culture dishes. After various treatments, the cells were washed with PBS and harvested. Next, mitochondria of Hepa1-6 were observed via a transmission electron microscope (TEM, Tecnai G2 F20, FEI, USA).

*In Vitro ICD Effect*: Hepa1-6 cells were seeded into 12-well plates and cultured for 24 h. After various treatments, cell supernatants were collected to determine ATP and HMGB1, and the cells were washed with PBS and harvested to measure CRT. ATP and HMGB1 were measured via an ATP kit and an HMGB1 Elisa kit, respectively. The CRT level was detected using flow cytometry.

*In Vivo Tumor Inhibition*: For early-stage HCC study: The left liver of the C57BL/6 mice was inoculated with $1 \times 10^6$ Hepa1-6-Luc cells. The mice with hepatic tumors were treated by intragastric injections of drugs 3 days after inoculation. Six groups of mice were separately given distilled water, free Sor/Sal (Sor: 30 mg $kg^{-1}$, Sal: 5 mg $kg^{-1}$), PEG-NP@Sor/Sal (Sor: 30 mg $kg^{-1}$, Sal: 5 mg $kg^{-1}$), BU-NP@Sor (Sor: 30 mg $kg^{-1}$), BU-NP@Sal (Sal: 5 mg $kg^{-1}$), or BU-NP@Sor/Sal (Sor: 30 mg $kg^{-1}$, Sal: 5 mg $kg^{-1}$) every other day for a total of five administration. The tumor growth was determined using IVIS (PerkinElmer) every 3 days, and the survival was recorded. Some mice were sacrificed 21 days after inoculation, and their blood, organs, and tumors collected for ferroptosis and toxicity evaluation.

For immune study: Three days after therapy, the blood and liver with tumor of mice were collected. Subsequently, the $CD4^+$ T cell, $CD8^+$ T cell, and activated DCs were measured using flow cytometry. The TNF-$\alpha$, IL-12, TGF-$\beta$, and IL-10 levels were detected via Elisa kits.

For immune memory study: The mice inoculated with Hepa1-6-Luc cells were treated with distilled water or BU-NP@Sor/Sal. Three days after the treatment, $5 \times 10^6$ Hepa1-6-Luc cells were inoculated subcutaneously. The tumor volume was determined using a vernier caliper every 2 days. The mice were sacrificed 16 days after the rechallenge for blood and spleen collection and subsequently for immune memory evaluation.

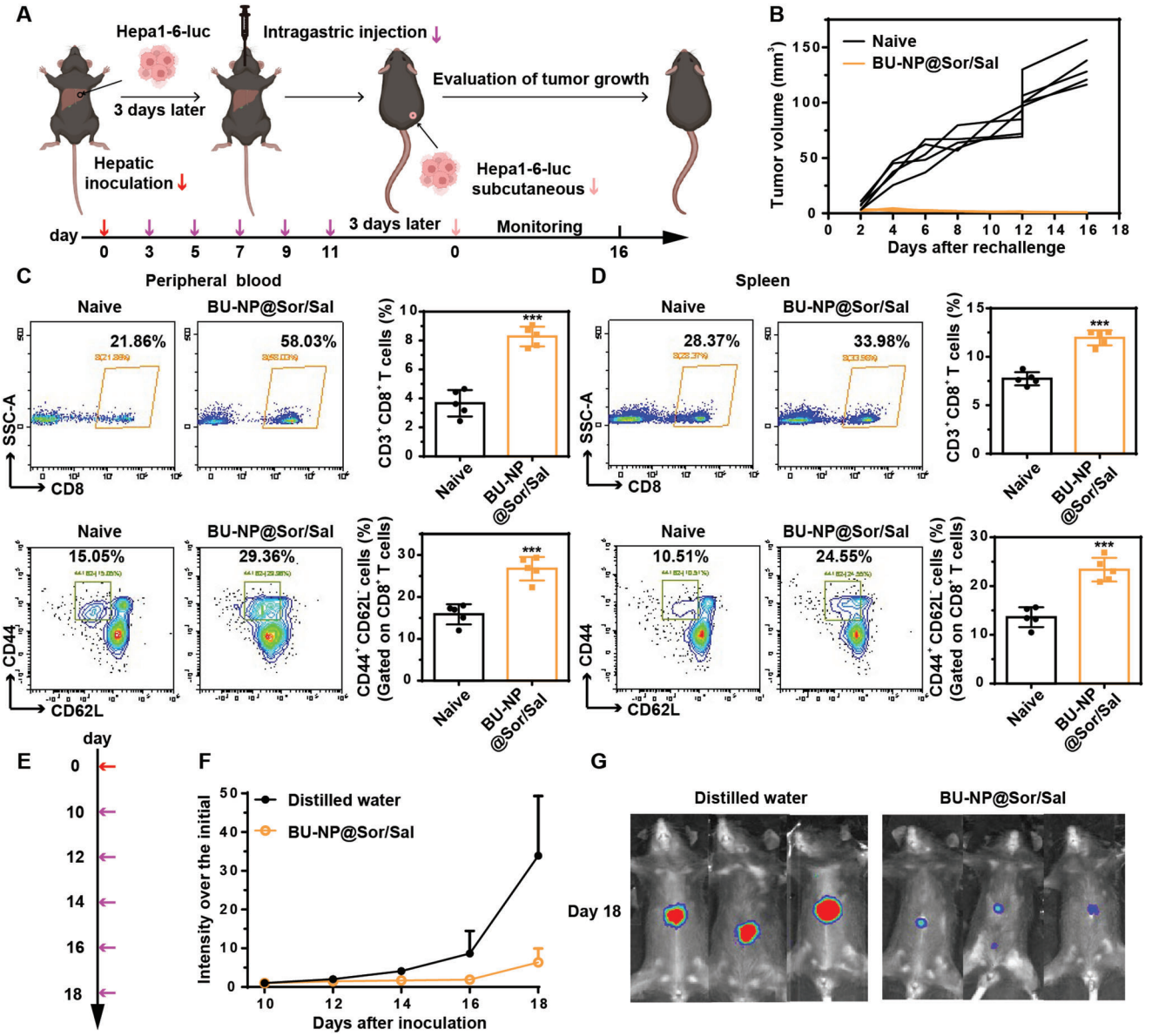


**Figure 8.** The combination of BU-NP@Sor and BU-NP@Sal showed immune surveillance and inhibited tumor growth in advanced HCC. A) Schematic illustration of tumor rechallenge experiment. B) Tumor growth curves. Frequency of $CD8^+$ T cells and $CD44^+$ $CD62L^-$ memory effector $CD8^+$ T cells in the peripheral blood (C) and spleen (D). E) Schematic illustration of tumor inoculation and treatment in the advanced stage. F) Tumor growth curves. G) Bioluminescence imaging of tumor-bearing mice. ***$p<0.001$, mean ± SD ($n = 5$).

For advanced stage HCC study: Ten days after Hepa1-6-Luc cells inoculation, intervention was applied. Two groups of mice were given distilled water and BU-NP@Sor/Sal, respectively. The tumor growth was determined using IVIS (PerkinElmer) every 2 days.

## Supporting Information

Supporting Information is available from the Wiley Online Library or from the author.

## Acknowledgements

The authors acknowledge financial support from the National Natural Science Foundation for Regional Innovation and Development (U22A20356), the National Key R&D Program of China (2021YFE0115200).

## Conflict of Interest

The authors declare no conflict of interest.

## Data Availability Statement

The data that support the findings of this study are available from the corresponding author upon reasonable request.

## Keywords

butyrate, ferroptosis, hepatocellular carcinoma, nanoparticles, oral delivery

Received: February 8, 2023
Revised: April 2, 2023
Published online: May 10, 2023

[1] J. M. Llovet, R. K. Kelley, A. Villanueva, A. G. Singal, E. Pikarsky, S. Roayaie, R. Lencioni, K. Koike, J. Zucman-Rossi, R. S. Finn, *Nat. Rev. Dis. Primers* **2021**, *7*, 6.
[2] A. Vogel, T. Meyer, G. Sapisochin, R. Salem, A. Saborowski, *Lancet* **2022**, *400*, 1345.
[3] J. Fu, H. Wang, *Cancer Lett* **2018**, *412*, 283.
[4] N. K. Mohamed, M. A. Hamad, M. Z. E. Hafez, K. L. Wooley, M. Elsabahy, *Int. J. Cancer* **2016**, *140*, 1475.
[5] X. Jiang, B. R. Stockwell, M. Conrad, *Nat. Rev. Mol. Cell Biol.* **2021**, *22*, 266.
[6] D. Tang, X. Chen, R. Kang, G. Kroemer, *Cell Res.* **2021**, *31*, 107.
[7] L. Li, X. Wang, H. Xu, X. Liu, K. Xu, *Front. Mol. Biosci.* **2022**, *9*, 1.
[8] M. Kudo, *Liver Cancer* **2015**, *4*, 39.
[9] M. Kudo, R. S. Finn, S. Qin, K. Han, K. Ikeda, F. Piscaglia, A. Baron, J. Park, G. Han, J. Jassem, J. F. Blanc, A. Vogel, D. Komov, T. R. J. Evans, C. Lopez, C. Dutcus, M. Guo, K. Saito, S. Kraljevic, T. Tamai, M. Ren, A. Cheng, *Lancet* **2018**, *391*, 1163.
[10] T. E. Hutson, S. Al-Shukri, V. P. Stus, O. N. Lipatov, Y. Shparyk, A. H. Bair, B. Rosbrook, G. I. Andrews, N. J. Vogelzang, *Clin. Genitourin. Canc.* **2017**, *15*, 72.
[11] T. Lin, D. Gao, Y. Liu, Y. Sung, D. Wan, J. Liu, T. Chiang, L. Wang, Y. Chen, *J. Controlled Release* **2016**, *221*, 62.
[12] T. Liu, W. Liu, M. Zhang, W. Yu, F. Gao, C. Li, S. Wang, J. Feng, X. Zhang, *ACS Nano* **2018**, *12*, 12181.
[13] W. Fan, Q. Wei, J. Xiang, Y. Tang, Q. Zhou, Y. Geng, Y. Liu, R. Sun, L. Xu, G. Wang, Y. Piao, S. Shao, Z. Zhou, J. Tang, T. Xie, Z. Li, Y. Shen, *Adv. Mater.* **2022**, *34*, 2109189.
[14] J. Y. Lock, T. L. Carlson, R. L. Carrier, *Adv. Drug Delivery Rev.* **2018**, *124*, 34.
[15] J. E. V. Ramirez, L. A. Sharpe, N. A. Peppas, *Adv. Drug Delivery Rev.* **2018**, *139*, 158.
[16] L. Wu, M. Liu, W. Shan, X. Zhu, L. Li, Z. Zhang, Y. Huang, *J. Controlled Release* **2017**, *262*, 273.
[17] L. Wu, Y. Bai, M. Liu, L. Li, W. Shan, Z. Zhang, Y. Huang, *Mol. Pharmaceut.* **2018**, *15*, 4273.
[18] V. L. Payen, E. Mina, V. F. V. Hée, P. E. Porporato, P. Sonveaux, *Mol. Metab.* **2020**, *33*, 48.
[19] Y. Yu, L. Xing, L. Li, J. Wu, J. He, Y. Huang, *J. Controlled Release* **2021**, *341*, 215.
[20] T. T. Mai, A. Hamaï, A. Hienzsch, T. Cañeque, S. Müller, J. Wicinski, O. Cabaud, C. Leroy, A. David, V. Acevedo, A. Ryo, C. Ginestier, D. Birnbaum, E. Charafe-Jauffret, P. Codogno, M. Mehrpour, R. Rodriguez, *Nat. Chem.* **2017**, *9*, 1025.
[21] W. S. Yang, B. R. Stockwell, *Trends Cell Biol.* **2016**, *26*, 165.
[22] D. Zheng, Q. Lei, J. Zhu, J. Fan, C. Li, C. Li, Z. Xu, S. Cheng, X. Zhang, *Nano Lett.* **2017**, *17*, 284.
[23] Y. Yu, S. Li, Y. Yao, X. Shen, L. Li, Y. Huang, *Bioact Mater* **2023**, *20*, 539.
[24] S. Ahadian, J. A. Finbloom, M. Mofidfar, S. E. Diltemiz, F. Nasrollahi, E. Davoodi, V. Hosseini, I. Mylonaki, S. Sangabathuni, H. Montazerian, K. Fetah, R. Nasiri, M. R. Dokmeci, M. M. Stevens, T. A. Desai, A. Khademhosseini, *Adv. Drug Delivery Rev.* **2020**, *157*, 37.
[25] X. Song, R. Li, H. Deng, Y. Li, Y. Cui, H. Zhang, W. Dai, B. He, Y. Zheng, X. Wang, Q. Zhang, *Biomaterials* **2018**, *180*, 78.
[26] T. Chou, P. Talalay, *Adv Enzyme Regul* **1984**, *22*, 27.
[27] S. Zanganeh, G. Hutter, R. Spitler, O. Lenkov, M. Mahmoudi, A. Shaw, J. S. Pajarinen, H. Nejadnik, S. Goodman, M. Moseley, L. M. Coussens, H. E. Daldrup-Link, *Nat. Nanotechnol.* **2016**, *11*, 986.
[28] C. Xue, M. Li, Y. Zhao, J. Zhou, Y. Hu, K. Cai, Y. Zhao, S. Yu, Z. Luo, *Sci. Adv.* **2020**, *6*, eaax1346.
[29] A. Hamaï, T. Cañeque, S. Müller, T. T. Mai, A. Hienzsch, C. Ginestier, E. Charafe-Jauffret, P. Codogno, M. Mehrpour, R. Rodriguez, *Autophagy* **2017**, *13*, 1465.
[30] X. Meng, D. Li, L. Chen, H. He, Q. Wang, C. Hong, J. He, X. Gao, Y. Yang, B. Jiang, G. Nie, X. Yan, L. Gao, K. Fan, *ACS Nano* **2021**, *15*, 5735.
[31] S. Xie, W. Sun, C. Zhang, B. Dong, J. Yang, M. Hou, L. Xiong, B. Cai, X. Liu, W. Xue, *ACS Nano* **2021**, *15*, 7179.
[32] Z. Zhou, H. Liang, R. Yang, Y. Yang, J. Dong, Y. Di, M. Sun, *Angew. Chem., Int. Ed.* **2022**, *61*, e202202843.
[33] C. Hetz, S. Saxena, *Nat. Rev. Neurol.* **2017**, *13*, 477.